Empirical Mode Decomposition of the Atmospheric Flows and Pollutant Transport over Real Urban Morphology

Yixun Liu[1], Chun-Ho Liu[1,*], Guy P. Brasseur[2,3,4] and Christopher Y.H. Chao[5,6]

[1]Department of Mechanical Engineering, The University of Hong Kong, Hong Kong

[2]Department of Civil and Environmental Engineering, The Hong Kong Polytechnic University, Hung Hom, Kowloon, Hong Kong

[3]National Center for Atmospheric Research, Boulder, CO, USA

[4]Max Planck Institute for Meteorology, Hamburg, Germany

[5]Department of Building Environment and Energy Engineering, The Hong Kong Polytechnic University, Hung Hom, Kowloon, Hong Kong

[6]Department of Mechanical Engineering, The Hong Kong Polytechnic University, Hung Hom, Kowloon, Hong Kong

Revised Manuscript No. ENVPOL-D-23-01839R1
submitted to
Environmental Pollution
on
May 15, 2023

**Corresponding author address:*

Chun-Ho LIU

Department of Mechanical Engineering
7/F, Haking Wong Building
The University of Hong Kong
Pokfulam Road, Hong Kong, CHINA
Tel: +852 3917 7901 / +852 9788 7951
Fax: +852 2858 5415
Email: liuchunho@graduate.hku.hk
https://aplhk.tech
ORCID: 0000-0002-4609-524X

Abstract

The momentum transport and pollutant dispersion in the atmospheric surface layer (ASL) are governed by a broad spectrum of turbulence structures. Whereas, their contributions have not been explicitly investigated in the context of real urban morphology. This paper aims to elucidate the contributions from different types of eddies in the ASL over a dense city to provide the reference of urban planning, realizing more favorable ventilation and pollutant dispersion. The building-resolved large-eddy simulation dataset of winds and pollutants over the Kowloon downtown, Hong Kong, is decomposed into a few intrinsic mode functions (IMFs) via empirical mode decomposition (EMD). EMD is a data-driven algorithm that has been successfully implemented in many research fields. The results show that four IMFs are generally enough to capture most of the turbulence structures in real urban ASL. In particular, the first two IMFs, which are initiated by individual buildings, capture the small-scale vortex packets that populate within the irregular building clusters. On the other hand, the third and fourth IMFs capture the large-scale motions (LSMs) detached to the ground surface that are highly efficient in transport. They collectively contribute to nearly 40% of vertical momentum transport even with relatively low vertical turbulence kinetic energy (TKE). LSMs are long, streaky structures that mainly consist of streamwise TKE components. It is found that the open areas and regular streets promote the portion of streamwise TKE in LSMs, improving the vertical momentum transport and pollutant dispersion. In addition, these streaky LSMs are found to play a crucial role in pollutant dilution in the near field after the pollutant source, while the small-scale vortex packets are more efficient in transport in the mid-field and far-field. (Word count: 276)

Keywords: Attached Eddies, Empirical Mode Decomposition, Large-Eddy Simulation, Large-Scale Motions, Pollutant Dispersion, and Turbulence Structures.

1. Introduction

The urban environment has been recognized as a serious, worldwide health concern because of the continuous increases in buildings and population. In particular, the air quality in cities has raised more public attention recently. It is estimated that air pollution is responsible for millions of premature deaths annually (Forouzanfar et al. 2016, Shrivastava et al. 2016). As such, it is of considerable importance to advance our understanding of ventilation and pollutant dispersion in the atmospheric surface layer (ASL) over urban areas (Lateb et al. 2016).

The turbulence structures in the atmospheric surface layer (ASL) govern the transport of momentum, gaseous pollutants, heat, particulate matter, and aerosol (Li et al. 2006, Gousseau et al. 2012, Tominaga et al. 2013, Zhong et al. 2015, Hang et al. 2017). However, the massive construction in urban areas slows down the winds that complicate the turbulence structures. For example, the inertial sublayer (ISL) away from the buildings is rather homogenous and therefore can be modeled empirically. However, the roughness sublayer (RSL) is affected tightly by the underlying buildings (Mo et al. 2021). It is inhomogeneous hence calls for a building-resolved description of the dynamics.

Recent progress in computation science and measurement techniques has enabled a detailed description of ASL over real urban morphology, in which a multitude of coexisting turbulence structures renders the velocity energy spectrum from viscosity scales to integral length scales (Fesquet et al. 2009, Inagaki et al. 2017, Zhang et al. 2019, Auvinen et al. 2020, Li et al. 2021, Liu et al. 2023a). In particular, a range of experiments (Michioka et al. 2011, Perret et al. 2013, Wang et al. 2014, Tang et al. 2019, Kim et al. 2020), field measurements (Wang et al. 2016, Liu et al. 2019), and numerical models (Mathis et al. 2009, Fang et al. 2015, Salesky et al. 2018, Jacobi et al. 2021) have consistently confirmed the existence of the large-scale (LSM) and very large-scale (VLSM) motions, whose streamwise wavelength λ_x could be as large as 20 times of the turbulent boundary layer (TBL) thickness δ. Meanwhile, the turbulence structure can be classified by its shape. Based on the attached eddy hypothesis (Townsend 1976), Hwang (2015) and Cheng et al. (2019) have concluded that one single attached eddy in the equilibrium TBL should consist of two distinct components. The first one is a long streaky structure whose streamwise λ_x and spanwise λ_y wavelengths follow

$$\lambda_x \approx 10\lambda_y . \tag{1}$$

This geometrical property is nearly identical to that proposed by Jiménez (2018) ($\lambda_x \sim 8\lambda_y$). The second component is a specific kind of vortex packet that carries all three components of fluctuating velocity. It is also known as "attached clusters" (del ÁLamo et al. 2006) or "short and tall vortex packet" (Hwang 2015). Its wavelength in the streamwise and spanwise direction is described as

$$2\lambda_y \le \lambda_x \le 5\lambda_y \tag{2}$$

that has been verified by several smooth-wall simulations (Lee et al. 2014, Cheng et al. 2019, Deshpande et al. 2019, Hu et al. 2020).

In this study, we critically examine the ASL turbulence structures over urban areas together with their contribution to momentum transport and pollutant dispersion via decomposing the dynamics into a range of turbulence structures by empirical mode decomposition (EMD). An area source with constant pollutant concentration is placed upstream of downtown Kowloon peninsula, Hong Kong in the large-eddy simulation (LES). The LES calculates the velocity and pollutant concentrations in the street canyons with buildings resolved. The fluctuations of velocity and pollutant concentration are decomposed into a series of intrinsic mode functions (IMFs) simultaneously based on the multivariable EMD technique (Wang et al. 2017, Thirumalaisamy et al. 2018, Wang et al. 2019). The motion scales, energy contents, momentum transport, and pollutant dispersion driven by the full spectrum of eddies are critically examined.

2. Methodology

2.1 Governing Equation

LES of isothermal, incompressible flows is adopted in our study. Its principal idea is to reduce the computational cost by modeling the small turbulence scales, which are isotropic but most computationally demanding to be resolved, via filtering the Navier–Stokes equations spatially. As such, the resolved-scale continuity is

$$\frac{\partial \tilde{u}_i}{\partial x_i} = 0 \tag{3}$$

and the resolved-scale momentum conservation is

$$\frac{\partial \tilde{u}_i}{\partial t} + \frac{\partial}{\partial x_j} \tilde{u}_i \tilde{u}_j = -\frac{\partial \tilde{p}}{\partial x_i} - \frac{\partial \tau_{ii}}{\partial x_i} - \frac{\partial \tau_{ij}}{\partial x_j} . \tag{4}$$

The tilde $\tilde{\psi}$ denotes the spatial filter arriving the LES resolvable scales. Here, $\tilde{u}_i = \left(\tilde{u}, \tilde{v}, \tilde{w}\right)$ refers to the resolved-scale velocity components in the streamwise x, spanwise y, and vertical z direction of the Cartesian coordinates x_i, respectively, t the time, and p the kinematic pressure. The summation convention on repeated indices (i, j = 1, 2 and 3) applies. The unresolvable subgrid-scale (SGS) momentum flux

$$\tau_{ij} = \widetilde{u_i u_j} - \tilde{u}_i \tilde{u}_j = -\nu_{SGS} \left(\frac{\partial \tilde{u}_i}{\partial x_j} + \frac{\partial \tilde{u}_j}{\partial x_i} \right) + \frac{2}{3} k_{SGS} \delta_{ij} \tag{5}$$

are modeled by the Smagorinsky model (Smagorinsky 1963). Here,

$$\nu_{SGS} = C_k k_{SGS}^{1/2} \Delta \tag{6}$$

is the SGS kinematic viscosity, C_k (= 0.07) the Smagorinsky constant, Δ (= $\Delta\Omega^{1/3}$) the LES filter width, and $\Delta\Omega$ the volume of computation cell (Deardorff 1970). The one-equation SGS

TKE model (Yoshizawa et al. 1985)

$$\frac{\partial k_{SGS}}{\partial t}+\frac{\partial}{\partial x_i}k_{SGS}\tilde{u}_i=-\frac{1}{2}\tau_{ij}\frac{\partial \tilde{u}_i}{\partial x_j}+\frac{\partial}{\partial x_i}\left(\nu_{SGS}\frac{\partial k_{SGS}}{\partial x_i}\right)-C_\varepsilon\frac{k_{SGS}^{3/2}}{\Delta} \tag{7}$$

is adopted to handle the SGS TKE conservation where C_ε (= 1.05) is the modeling constant for the dissipation term. Inert pollutants, for instance, carbon monoxide (CO) or aerosol with neglectable buoyancy, are considered. As such, their transport is governed by

$$\frac{\partial \tilde{c}}{\partial t}+\frac{\partial}{\partial x_i}\tilde{c}\tilde{u}_i=-\frac{\nu_{SGS}}{Sc}\frac{\partial \tilde{c}}{\partial x_i}, \tag{8}$$

where $\tilde{c}$ is the resolvable pollutant concentration and Sc (= 0.72) the Schmidt number.

2.2 Numerical Method

The governing equations are solved by the open-source finite volume code OpenFOAM-V1806 (OpenFOAM 2022). The implicit, first-order-accurate backward differencing is used in the time integration. The gradient term is handled by the second-order-accurate Gaussian finite volume method (FVM) integration of cell-limited gradient scheme and the divergence term is solved by the limited linear divergence scheme. The pressure-velocity coupling is solved by the combination of pressure implicit with the splitting of operator (PISO) and semi-implicit method for pressure-linked (SIMPLE) algorithm. After the geometric algebraic multigrid (GAMG) preconditioner, the symmetric equation systems are solved by the conjugate gradient (CG) method. Likewise, the asymmetric equation systems are preconditioned by the simplified diagonal-based incomplete, lower and upper triangular matrices (DILU) then are solved by the bi-conjugate gradient (BiCG) method.

The mathematical model is integrated for 6,000 seconds to initialize the flows and pollutant dispersion. After reaching the quasi-steady state, another 10,800 seconds ($180H_{ave}/u_\tau$)

of digital output data are recorded for analyses that are sufficiently long for statistical convergence (Bernardini et al. 2014, Vinuesa et al. 2016). Here, H_{ave} (= 36 m) is the mean building height and u_τ (= 0.59 m sec^{-1}) is the spatially averaged friction velocity of the entire computation domain. It is noteworthy that the local friction velocity is in the range of 0.5 m sec^{-1} $\leq u_\tau \leq$ 0.6 m sec^{-1}, depending on the surface roughness (Yao et al. 2022).

2.3 Boundary Conditions and Computation Domain

The downtown Kowloon Peninsula, Hong Kong (Figure 1a), where is a dense urban region, is discretized by almost 10 million finite volume cells (FVCs). The computation domain (Figure 1b), whose streamwise x, spanwise y, and vertical z direction, has respective spatial extents of 5,440 m (L_x), 1,230 m (L_y), and 2,000 m (L_z). The near-ground region with dense buildings is refined by a grid stretching from 1:2 to 1:4 to improve the spatial resolution. The characteristic FVC size Δ (= $\Delta\Omega^{1/3}$) ranges from 0.65 m to 60 m. In the near-ground regions ($z \leq 100$ m; Figure 1c), the characteristic size Δ is around meters whose 5%, 50%, and 95% percentiles are 3.08 m, 3.81 m, and 4.22 m, respectively. This resolution also fulfills the practical guidelines (Tominaga et al. 2008) in which 1/10 of the characteristic building size is suggested (equal to mean building height H_{ave} = 36 m in this study). The criterion of the Courant Friedrichs-Lewy (CFL) number is ensured by setting the time step Δt = 0.02 sec. The wall function follows Spalding (1962) which is applicable throughout laminar and turbulent flow regimes.

The wind speeds at the inlet boundary are prescribed by

$$\tilde{u} = U_s \times \left(\frac{z}{z_s} \right)^{1/5} \quad \text{and} \quad \tilde{v} = \tilde{w} = 0, \tag{9}$$

where U_s is the average wind speed at the reference height z_s (= 300 m). The outlet boundary condition (BC) is non-reflective for flow and pollutant so they do not bounce back. The domain top and the lateral boundaries are symmetry BCs for flow and zero-gradient for pollutant. Both the building facades and the natural terrains are set to no-slip solid walls for flow and zero-gradient for pollutant. The freestream wind speed at the domain top is U_∞ = 10 m sec^{-1} and the maximum building height H_{max} is 180 m. Hence, the Reynolds number Re (= $U_\infty H_{max}/\nu$) exceeds 10^8, satisfying the Reynolds number independence.

The TBL height δ (= 330 m), RSL top (z_{RSL} = 95 m), and ISL top (z_{ISL} = 228 m) are all determined based on our previous work (Yao et al. 2022, Liu et al. 2023c). The area source of inert pollutants is placed in the upstream region of the computation domain. Constant pollutant concentration C_0 (= 1,000 ppm) is set at the source to simulate the accidental gas leakage. The mesh independence was tested in our previous research (Cheng et al. 2021). No significant difference in the turbulence statistics was observed among different spatial resolutions. Moreover, the current LES results (Yao et al. 2022) are in line with those of wind tunnel observations (Mo et al. 2021). The flow near the inlet might not be fully developed due to the inlet BC. Therefore, the first 1,000 m is used for flow development. We perform the analysis downstream at least 1,000 m (27H_{ave}) after the inlet. According to similar studies of real urban morphology (Tominaga et al. 2008, Antoniou et al. 2017, Duan et al. 2021), this distance from the inlet is long enough to allow for full flow development. The intermittent LSMs/VLSMs over real urban morphology is frequently examined by wavelet (Lotfy et al. 2019, Auvinen et al. 2020, Horiguchi et al. 2022) whose instantaneous feature is suitable for capturing the intermittent LSMs/VLSMs. Liu et al. (2023a) investigated the energy spectrum of streamwise velocity and the detection of LSMs/VLSMs based on the LES dataset used in this study Moreover, wavelet was adopted to illustrate the influence of individual buildings on the intermittency of LSMs/VLSMs.

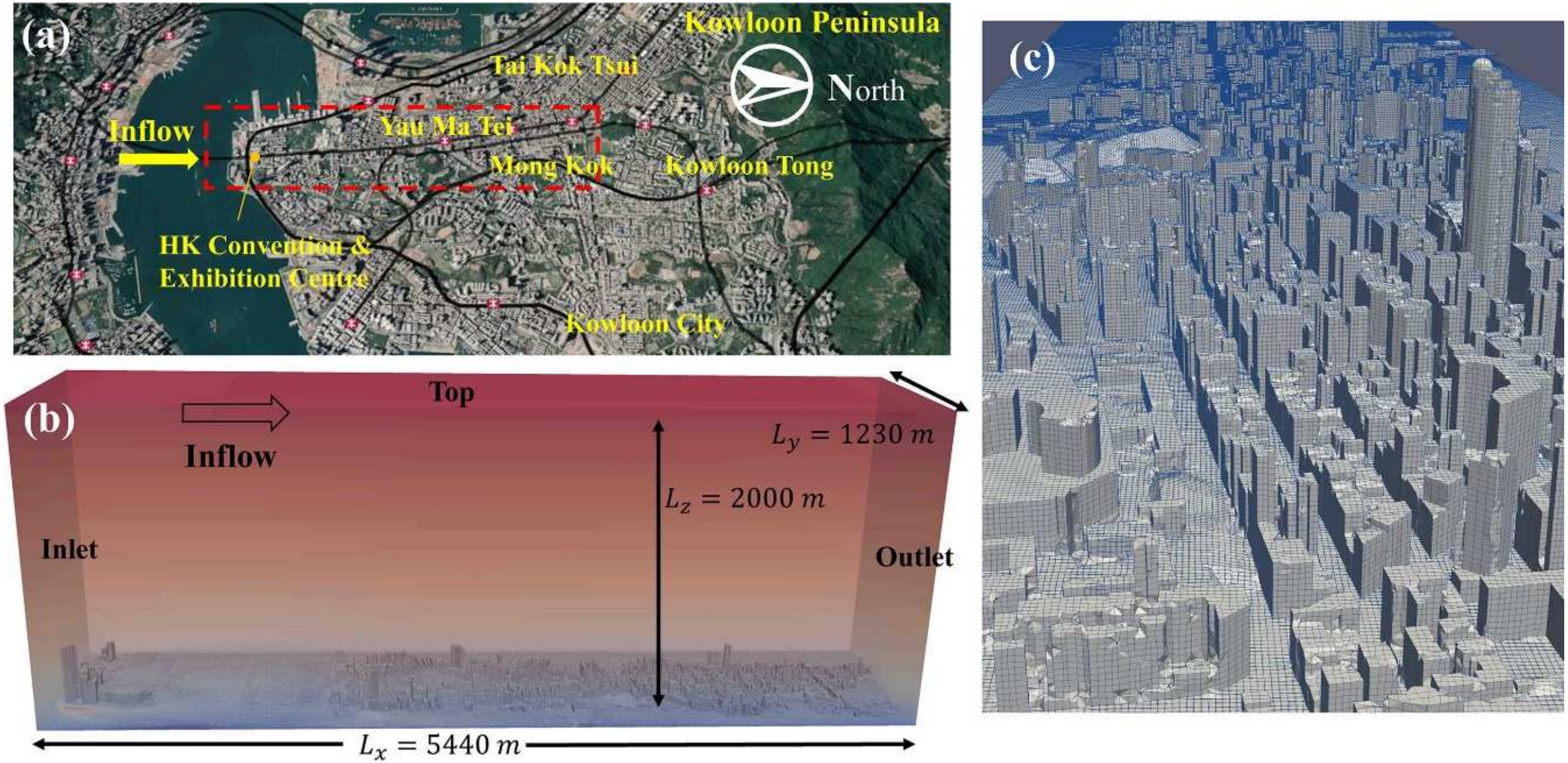

Figure 1. (a) Satellite image of downtown Kowloon Peninsula, Hong Kong from Google Maps. (b) LES Computation domain (Tsim Sha Tsui to Sham Shui Po). (c) Surface and building meshes in the near-ground region.

161

3. Theoretical Background

Effort has been sought to differentiate the contributions from motion scales to the turbulence kinetic energy (TKE), momentum flux, and pollutant transport (Held 2013, Lee et al. 2014, Wang et al. 2016, Auvinen et al. 2020, Encinar et al. 2020). For example, wavelet analysis was applied to detect the LSMs and VLSMs in field measurements (Fesquet et al. 2009, Horiguchi et al. 2012, Lotfy et al. 2019) in favor of providing the instantaneous energy spectra. When the LSMs or VLSMs pass by, (temporal) conditional sampling can be conducted to contrast the flow properties between LSMs and other small-scale eddies. Other methods, such as signal processing (low-pass filter), needs a pre-determined cutoff wavelength (frequency) to separate different motion scales. For example, the scale interaction between outer-layer VLSMs and inner-layer small-scale eddies is commonly investigated via a low-pass filter. Evidently, the small-scale eddies are amplitude modulated by VLSMs (Mathis et al. 2009, Talluru et al. 2014, Anderson 2016).

More recently, data-driven algorithms, such as proper orthogonal decomposition (POD), enable researchers to decompose the velocity field into a range of eddies ranked by their TKE contents (Jadidi et al. 2017, Tang et al. 2020, Masoumi-Verki et al. 2021, Liu et al. 2023b). In this connection, the contributions and properties of various eddies (represented by different modes) can be examined in detail. However, the (temporal) conditional sampling unavoidably mixed up the dominant LSMs with some unignorable small-scale components (Horiguchi et al. 2012, Auvinen et al. 2020). Tools for scale separation, such as wavelet, Fourier transform, or POD, need for a priori knowledge of cutoff standards to partition the eddies into different scales. However, the cutoff frequency (signal processing) or mode (POD) is determined mainly based on experience rather than the intrinsic data scale. In addition, the filter and POD hardly decompose the velocity or scaler fields (e.g., pollutant concentration or temperature) simultaneously. They are thus inadequate to investigate the coupling between flows and other variables.

EMD is another data-driven technique to decompose signals into IMFs. It has drawn keen attention lately in the areas of the economy, remote sensing, defect detection, oceanic boundary layer, and ASL (Oladosu 2009, Hawinkel et al. 2015, Meng et al. 2015, Gao et al. 2016, Martins et al. 2017). Compared with wavelet analysis, Fourier transform, or POD, EMD has several advantages. First, it is purely data-driven, so no pre-determined basis function (e.g., sinusoidal wave) is required to partition the motion scales. In fact, EMD solely bases on the characteristic space or time scales inherent in the data. Thus, the IMFs are adaptively biased toward locally dominant frequencies that enable the extraction of physically relevant processes in a finite bandwidth in a transient manner (Mäteling et al. 2020). Besides, EMD is able to decompose multiple fields (multivariate EMD; Rilling et al. 2007, Rehman et al. 2010, Lv et al. 2016, Wang et al. 2017, Thirumalaisamy et al. 2018, Wang et al. 2019) while preserving their intrinsic relationship/coupling. Therefore, the pollutant concentration can be decomposed along with the velocity field that enables a detailed investigation of the contribution from different turbulence structures to momentum transport and pollutant dispersion.

With recent progress in computer science and measurement technology, a detailed description of ASL flows over real urban morphology and the turbulence motion scales has been available (Antoniou et al. 2017, Aristodemou et al. 2018, Hertwig et al. 2019, Fu et al. 2020, Cheng et al. 2021, Yao et al. 2022, Zheng et al. 2021, Liu et al. 2023a). Those datasets enable the data-driven algorithm, such as EMD, to investigate the dynamics and their contributions to the transport processes. To the best knowledge of the authors, however, most EMD applications were based on smooth walls (Wang et al. 2017, Cheng et al. 2019) or idealized urban surfaces (Agostini et al. 2018). Its applications for real urban morphology are rather limited. EMD has been only utilized by a handful of researchers to investigate the contribution from different motion scales based on field measurement (Martins et al. 2016, Cheng et al. 2017), which, however, is limited to pointwise samples. Besides, the pollutant transport, which directly affects the air quality in street canyons, has not been examined in detail yet.

EMD was first introduced by Huang et al. (1998). It is a data-driven algorithm to decompose the input signal into the linear combination of a range of IMFs. In contrast to Fourier and wavelet analyses, EMD does not require any pre-determined basis functions. Instead, it directly extracts the IMFs based on the instantaneous features of the input signal. Therefore, it is a data-driven, a posteriori method for data analysis that minimizes the artificial numerical enforcement or truncation (Cheng et al. 2019).

We start with decomposing the time trace of streamwise fluctuating velocity $u'(t)$ to introduce the methodology of EMD. The steps involved in the IMF computation are as follows:

1. Find all the local maxima of $u'(t)$ then link them up with a smooth curve (e.g., cubic spline interpolating function) to form the upper envelope of the signal $u'_{up}(t)$. Correspondingly, the lower envelope $u'_{low}(t)$ is identified via the local minima.
2. Subtract the average envelope $u'_{ave}(t) = (u'_{up}(t) + u'_{low}(t))/2$ from the original signal $u'(t)$ to obtain the new data series $h(t) = u'(t) - u'_{ave}(t)$.
3. Replace $u'(t)$ by $h(t)$ in Step 1 and repeat the above steps until convergent at the k-th iteration according to the criterion (Huang et al. 1998, Cheng et al. 2019)

$$SD = \frac{\sum_{t=0}^{T} \left| u'_k(t) - u'_{k-1}(t) \right|^2}{\sum_{t=0}^{T} \left| u'_k(t) \right|^2} \leq 0.1. \tag{10}$$

Here, T is the total number of samples in the time trace. Once the convergence criterion is satisfied, the first IMF is defined as $IMF_1(t) = u'_k(t)$.

4. Afterward, IMF_1 is subtracted from the original signal $u'(t)$ to update the signal input $u'_{new}(t)$ ($= u'(t) - IMF_1(t)$). Steps 1 to 4 are then repeated until all the IMFs are derived.

After the converged iteration, the original time-trace signal $u'(t)$ is decomposed into a series of IMFs plus a residual $R(t)$, as follows

$$u'(t) = \sum_{i=1}^{m} IMF_i(t) + R(t). \tag{11}$$

An example of EMD is recorded in Appendix A. As the IMF (mode) number increases, the IMFs gradually shift from the local-scale information to the global one. Multivariate EMD, which was proposed by Rehman et al. (2010), is adopted in this study to decompose the fluctuating velocities u_i' (= (u', v', w')) and the fluctuating pollutant concentration c' simultaneously to elucidate the coupling (see Wang et al. 2017 and Thirumalaisamy et al. 2018 for details), examining the contribution to the fluxes of momentum $u'w'$ and pollutant $w'c'$ from different scales (IMFs).

4. Result and Discussion

4.1 Flow Field

Figure 2 presents the shaded contours of premultiplied energy spectrum $k_i \times \phi_{uiui}$ as functions of wavelength λ_i and elevation z. Here, the index i denotes the x, y, and z directions and k_i (= $2\pi/\lambda_i$) the wavenumber in the *i* direction. The shaded contours (white to black) and the solid lines (0.3:0.6:0.9 of IMFs) depict the premultiplied spectrum of the original signal (*u'*, *v'*, *w'*) and individual IMFs, respectively. In line with Agostini et al. (2018), Debert et al. (2010), and Fan et al. (2022), a few IMFs are sufficient to represent the original signal that carry most of the energy. In this case, only 4 modes can be universally detected in most locations while up to 6 modes can be found in some locations down in the RSL close to the buildings. For the sake of consistency, only the first four IMFs are shown in this paper. In particular, IMF_4 includes the contribution from and above the 4-th mode ($IMF_4 + IMF_5 + IMF_6$, if any) that signifies the global characteristic of the original signal (Cheng et al. 2019). The IMFs capture well the original fluctuations in different ranges of wavenumber because the contour lines of individual IMFs collectively cover the full spectrum of the original signals (Figure 2).

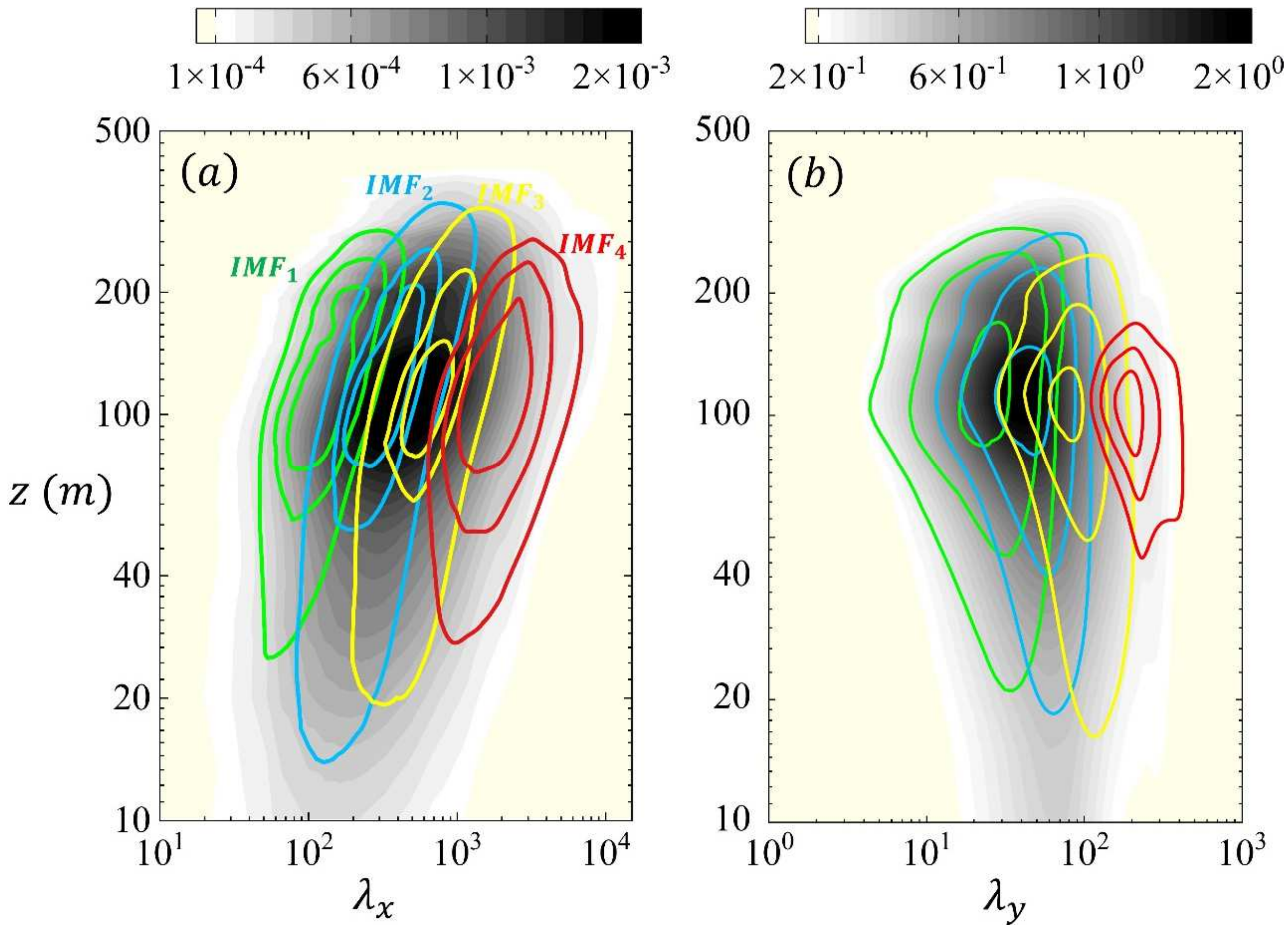

Figure 2. Shaded contours of premultiplied energy spectra $k_x \times \phi_{uu}$ and $k_y \times \phi_{vv}$ of (a) streamwise (u') and (b) spanwise (v') IMFs. The shaded contours (white-black) are premultiplied spectrum of original signal, and the solid lines represent the 0.3, 0.6, 0.9 maximum of individual IMF spectra.

267

The turbulence structures represented by IMFs illustrate a wide range of motion scales. Their dominant wavelength can be derived from the peaks of IMF energy spectra (Figure 2). The streamwise wavelengths λ_x of IMF_1 to IMF_4 dominate at 90 m, 250 m, 600 m, and 1,500 m, respectively. Analogously, the spanwise wavelengths λ_y of IMF_1 to IMF_4 dominate at 30 m, 50 m, 60 m, and 180 m, respectively. According to the streamwise wavelength λ_x, IMF_1 and IMF_2 can be classified as small-scale eddies ($\lambda_x < \delta$; where $\delta = 330$ m), while IMF_3 and IMF_4 LSMs ($\lambda_x > \delta$). In addition, based on the Townsend attached-wall hypothesis (Townsend 1976), IMF_1 and IMF_2 are vortex packets that carry the velocity fluctuations in all the three directions (Cheng et al. 2019, Hu et al. 2020) as their streamwise and spanwise wavelengths follow $2\lambda_y \leq \lambda_x \leq 5\lambda_y$ (Equation 2). In contrast, IMF_3 and IMF_4 are long streaky structures ($\lambda_x \approx 10\lambda_y$; Equation 1) that mainly carry streamwise velocity fluctuations. These two standards suggest a consistent classification. They in turn echo the simulation and measurement results in the literature that the long streaky structures ($\lambda_x \approx 10\lambda_y$) are mainly LSMs or even VLSMs (Lee et al. 2014, Hwang 2015, Cheng et al. 2019).

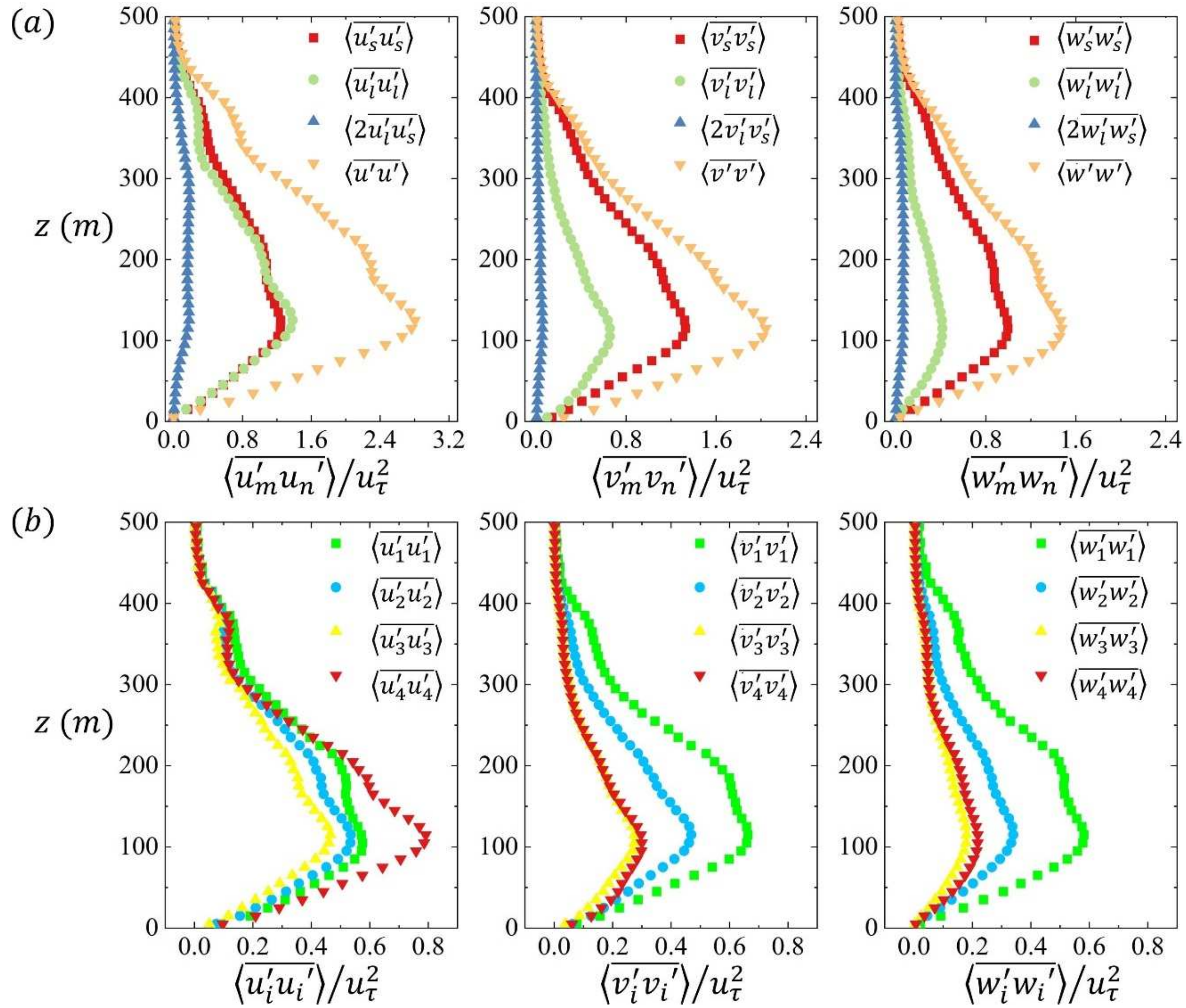

Figure 3. Ensemble average of dimensionless profiles of streamwise *u'*, spanwise *v'*, and vertical *w'* fluctuating velocities. (a) Contributions from small scales, large scales, and cross-scale interactions; together with (b) detailed contributions from different IMFs.

282

Figure 3 presents the ensemble average of the TKE contribution from different IMFs in the streamwise, spanwise, and vertical directions as functions of elevation z. The spatial average on the horizontal x-y plane is denoted by the angle brackets $\langle \psi \rangle$. The interaction between different scales illustrates a relatively small contribution because the correlation among different modes is generally weak due to different motion scales (Figure 3a). By contrast, the direct contribution from individual IMFs plays a dominant role in TKE (Figure 3b).

It is noteworthy that IMF_4 contributes far more in the streamwise direction than it does in the spanwise or vertical directions (Figure 3b). This echoes the conclusion from Hwang (2015) and Cheng et al. (2019). It is because the long-streaky (detached) structures in the IMF_4 mainly carry the streamwise velocity fluctuations. In contrast, IMF_1 and IMF_2 contribute more in the spanwise and vertical directions because they are the vortex packets containing all three components of velocity fluctuation. Besides, the LSMs contribute nearly 50% to the streamwise TKE component that is in line with the LSM contribution in open-channel flows (Duan et al. 2020).

Multivariable EMD separates the motion scales while keeps the inherent coupling among the variables. It enables the comparison of small-scale (u_s' and w_s') and large-scale (u_l' and w_l') contributions from fluctuating streamwise u' and vertical w' velocities to momentum transport. Figure 4a contrasts the vertical momentum flux contribution from small scale (IMF_1 and IMF_2; $\langle \overline{u_s' w_s'} \rangle$, large scale ($IMF_3$ and IMF_4; $\langle \overline{u_l' w_l'} \rangle$), together with their scale interaction ($\langle \overline{u_s' w_l'} \rangle$ and $\langle \overline{u_l' w_s'} \rangle$). In addition, Figure 4b details the contribution to momentum flux from different IMFs. It is noteworthy that the LSMs (IMF_3, $\lambda_x \geq 2\delta$) and VLSMs (IMF_4, $\lambda_x \geq 5\delta$) are responsible for nearly 40% of momentum transport $u'w'$. This finding echoes that the VLSMs are responsible for more than 40% momentum flux in open-channel-flow experiments (Duan et al. 2021). Moreover, Agostini et al. (2018) reported that the large-scale fluctuations are responsible, directly on their own, for roughly 30% to the skin friction. The current mathematical modeling result further supports the analogy of real urban morphology above the urban canopy layer (UCL) to their smooth-wall counterparts because of their similar turbulence structures and TKE contribution.

Figure 4c contrasts the correlation coefficient

$$r_{uw,IMF_i} = \frac{\left\langle \overline{u'w'} \right\rangle_{IMF_i}}{\left\langle \overline{u'u'} \right\rangle_{IMF_i}^{1/2} \left\langle \overline{w'w'} \right\rangle_{IMF_i}^{1/2}} \tag{12}$$

of different IMFs. In the RSL (95 m < z), $r_{uw,i}$ of all IMFs increases with increasing elevation because of eddy development. Apparently, IMF_3 (LSMs) and IMF_4 (VLSMs) show stronger (negative) correlations between the streamwise u and vertical w velocities. Given the comparable TKE contents in the streamwise $\left\langle \overline{u'u'} \right\rangle$ and vertical $\left\langle \overline{w'w'} \right\rangle$ direction, it is implied that large-scale eddies contribute more to the RSL momentum transport $\left\langle \overline{u'w'} \right\rangle$ than do their small-scale counterparts close to the buildings. That is also why the momentum flux of LSMs is found comparable to small-scale motions even the vertical TKE components are much less.

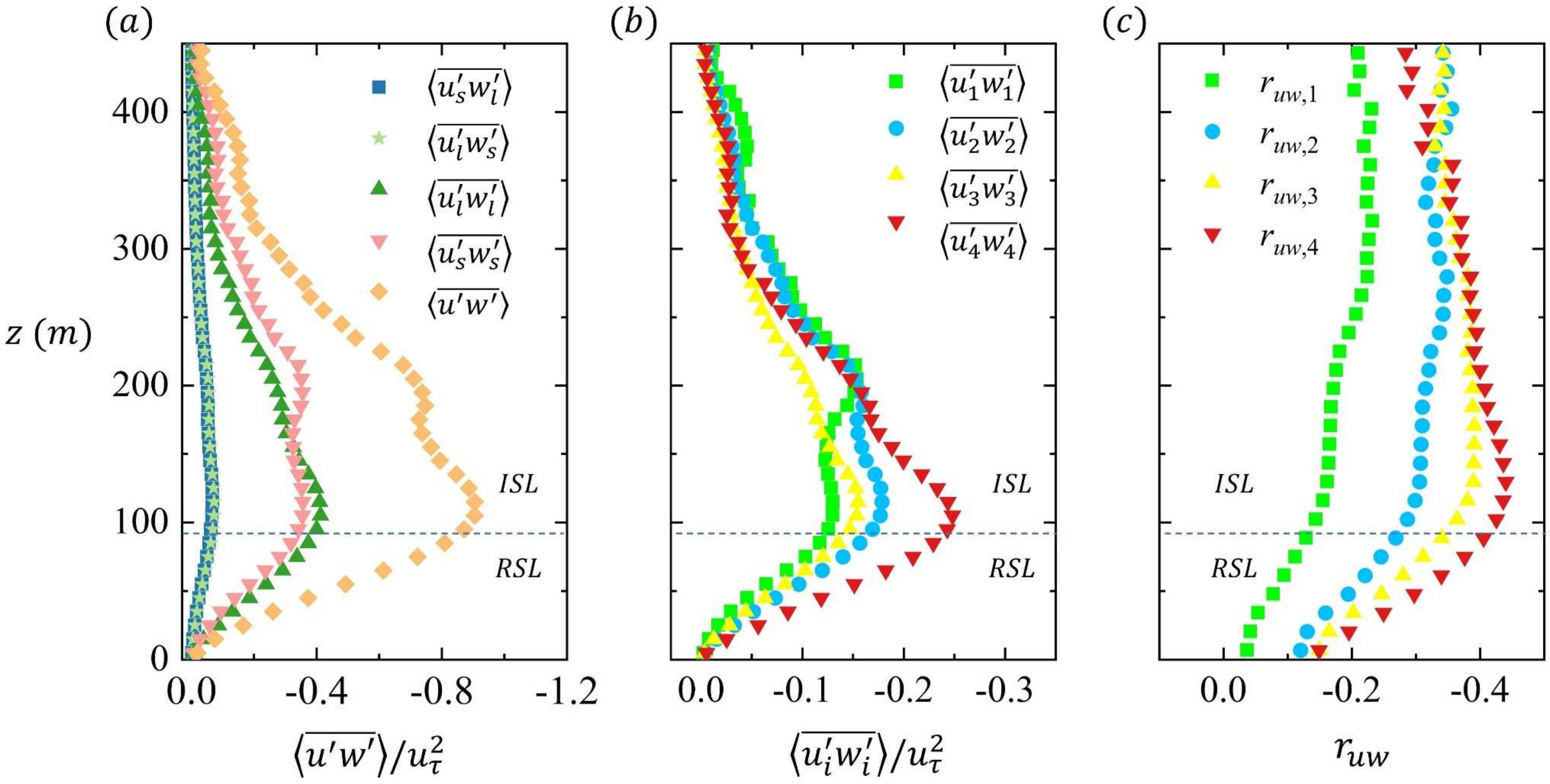

Figure 4. Momentum flux *u'w'* contribution from different IMFs. (a) Total contribution from different scales, (b) detailed contribution from different IMFs, and (c) the correlation coefficient r_{uw} of different IMFs.

322

Evidently, the large-scale momentum flux $\langle \overline{u_l' w_l'} \rangle$ outweighs the small-scale one $\langle \overline{u_s' w_s'} \rangle$ in the RSL (z < 95 m; Figure 4a). On the other hand, it is less than the small-scale transport in and above the ISL ($z \geq$ 95 m). This is one of key differences between the dynamics over smooth walls (Cheng et al. 2019) and real urban morphology with explicitly resolved buildings. In the smooth-wall configuration, small-scale and large-scale eddies populate in the near-wall and logarithmic (ISL) regions, respectively, dominating the transport. In real urban morphology, on the contrary, small-scale eddies are not only initiated by the ground surfaces (flow shear) but also by the heterogeneous buildings (flow impingements). These small-scale eddies would populate instantaneously above the RSL if they are initiated by high-rise buildings (building wakes). On the other hand, the channeling within street canyons (below UCL) enables the existence and development of LSMs in the near-ground region between two rows of buildings. The buildings and ground surface constitute open channels where the LSMs develop within, promoting the streamwise, long-streaky structures in UCLs.

Figure 5 further illustrates the existence of LSMs within the street canyons (channels) by contrasting the momentum flux contribution $S_{u'w'}$ from small-scale (= $\overline{u_s' w_s'} / \overline{u' w'}$; IMF_1 and IMF_2) and large-scale (= $\overline{u_l' w_l'} / \overline{u' w'}$; IMF_3 and IMF_4) motions at z = 50 m (in the RSL). As shown in Figure 5a, most contributions from small scales concentrate in the building near wakes, especially in some upstream regions, where the flows and turbulence are disturbed by staggering building clusters. In contrast, the contributions from large-scale eddies populate in the downstream street canyon, where the building layout is more uniform and regular. This finding once again illustrates the significance of LSMs in transport processes and the importance of proper urban planning in pedestrian-level ventilation to promote sustainability. Although substantial small-scale eddies could be initialized by staggered buildings, their transport efficiency is rather limited that could barely help the transport processes. On the other hand, the regular street canyons are spacious for eddy development. The dynamics are prominent especially for those long-streaky structures aligned in the streamwise direction that are beneficial for LSMs with remarkable transport efficiency.

4.2 Tracer Field

Figure 6a presents the distribution of time-averaged pollutant concentration $\overline{c}$ in the computation domain. The area source is located in -1,800 m $\leq x \leq$ -1,000 m at the ground level with a constant pollutant concentration c_0 = 1,000 ppm. The pollutant is prescribed as the inert tracer without buoyancy or chemical reaction. The region -500 m $\leq x \leq$ 500 m is prescribed as the near field, 500 m $\leq x \leq$ 1,500 m the mid field, and 1,500 m $\leq x \leq$ 2,500 m the far field, according to their distance after the pollutant area source. Figure 6b depicts the ensemble-averaged concentration $\left\langle \overline{c} \right\rangle / \left\langle \overline{c} \right\rangle_g$ normalized by the ground-level concentration $\left\langle \overline{c} \right\rangle_g$ as a function of elevation z. In the near field, most of the pollutant resides at the pedestrian level ($z \leq 50$ m) and the concentration drops significantly with increasing elevation thereafter. In the mid field and far field, on the contrary, more pollutant resides at higher elevation due to the turbulent dispersion in the vertical direction (Jiang et al. 2018, Wu et al. 2018).

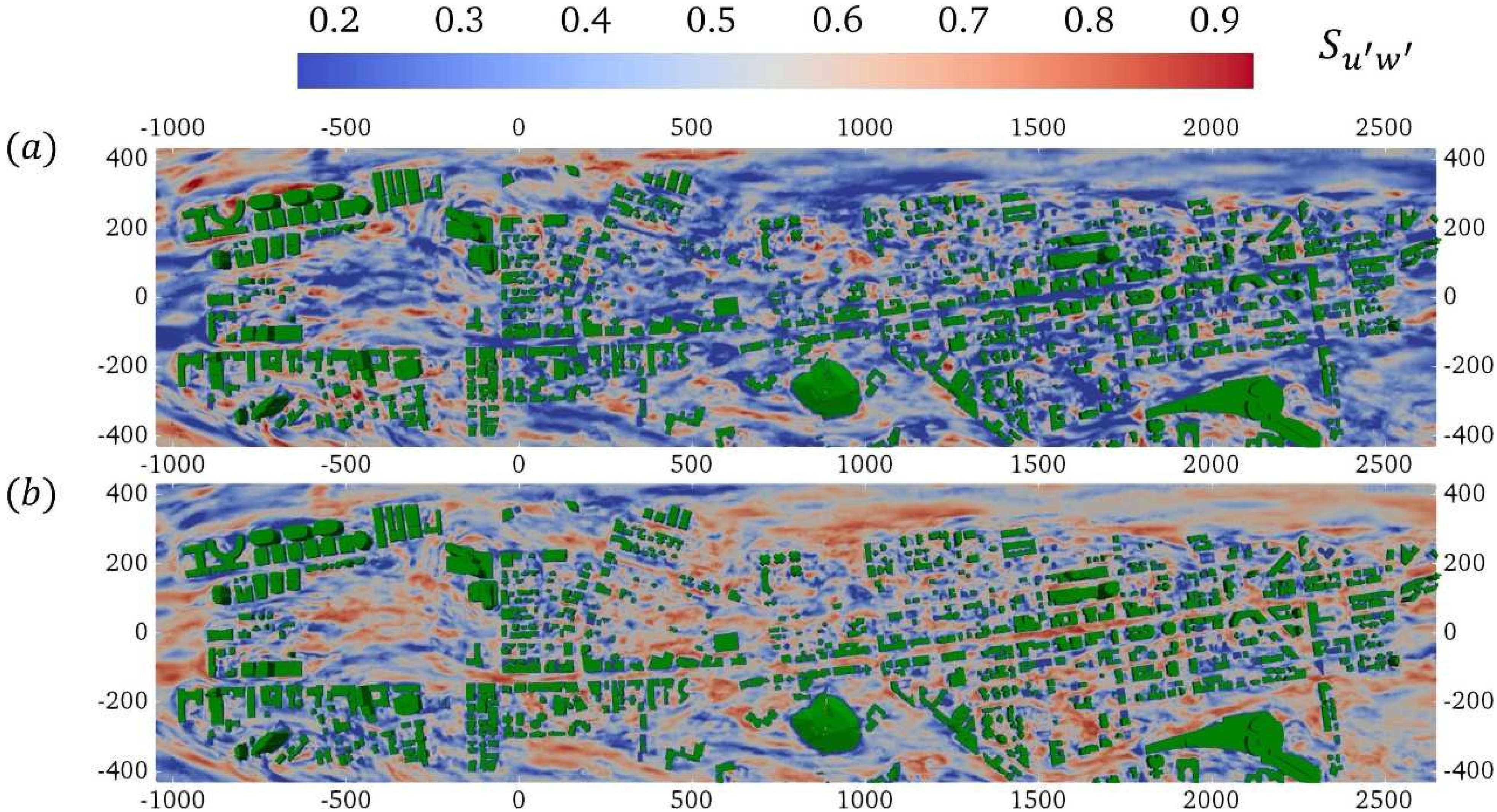

Figure 5. Horizontal view of the contribution $S_{u'w'}$ from (a) small $\overline{u_s'w_s'}/\overline{u'w'}$ and (b) large $\overline{u_l'w_l'}/\overline{u'w'}$ scales to momentum flux at z = 50 m (RSL).

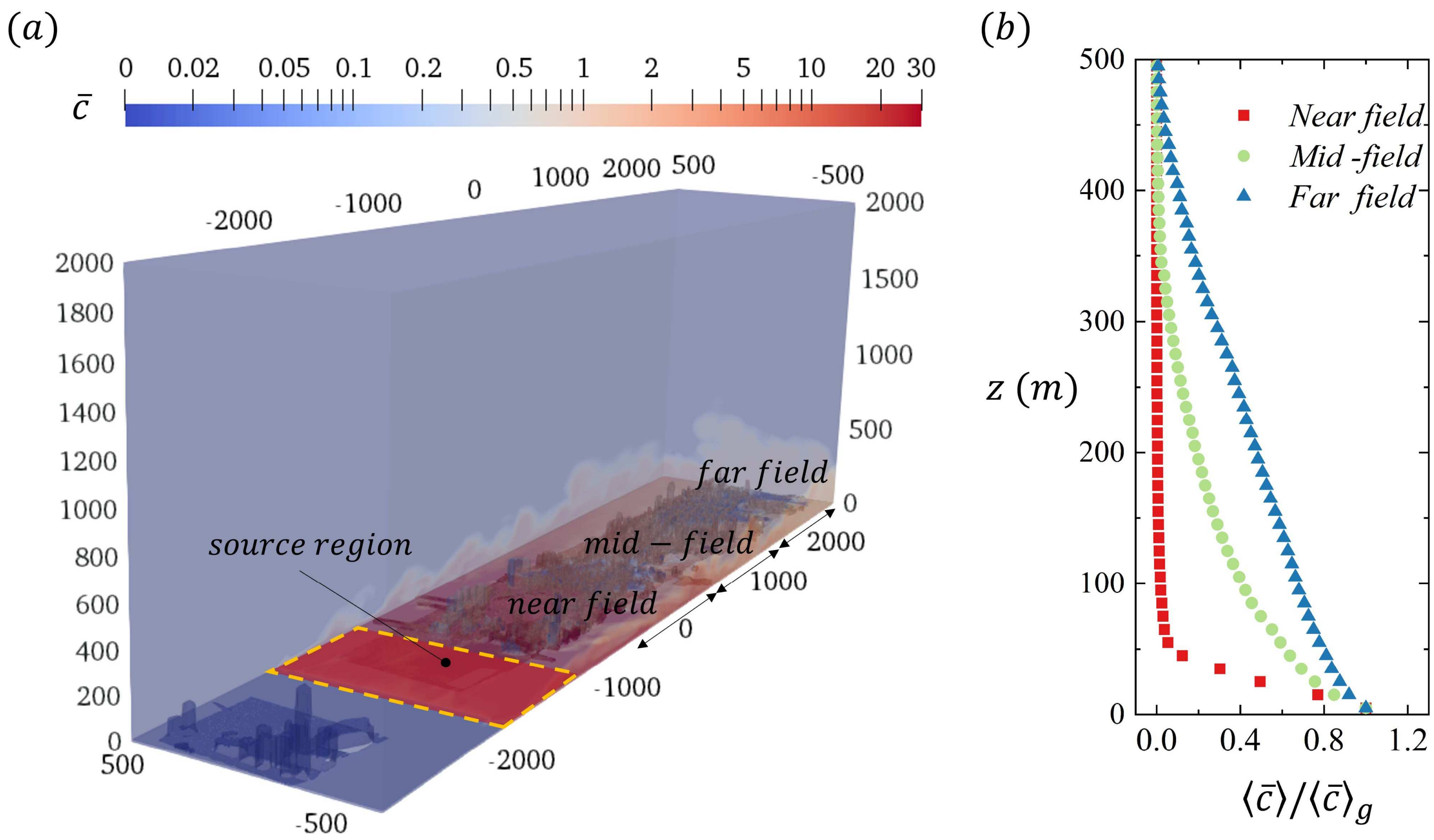

Figure 6. Pollutant concentration illustrated as the (a) spatial distribution of time average $\bar{c}$ and (b) ensemble averaged vertical profile $\langle \bar{c} \rangle / \langle \bar{c} \rangle_g$ normalized by the ground-level pollutant concentration $\langle \bar{c} \rangle_g$.

365

Figure 7a contrasts the pollutant flux contribution $\left\langle \overline{w'c'} \right\rangle$ between small and large scales, together with their interactions. It is shown that LSMs (IMF_3 + IMF_4) dominate the transport, especially in the near-field regions. Figure 7b further contrasts the pollutant flux contribution directly from individual IMFs. The peaked value of the original pollutant flux $<w'c'>_{max}$ is adapted for normalization. Obviously, the VLSMs (IMF_4) dominates the near-field pollutant transport. Other IMFs, however, have little contributions because they are substantially smaller than the plume coverage. In the far field, as the plume is continuously disrupted by the buildings and terrains, the pollutant concentration becomes inhomogeneous and the pollutant puff splits into small pieces. Therefore, all the four IMFs contribute comparably to the pollutant removal. IMF_3 and IMF_4 (LSMs) contribute more than 40% to total pollutant flux in the far field which is consistent with that in the momentum-flux contribution.

Compared with plume coverage, LSMs drive pollutant meandering/fluctuations (Gifford 1959, Csanady 1973, Franzese et al. 2007, Cassiani et al. 2009, Ardeshiri et al. 2020), i.e., large-scale ejection Q_2 and sweep Q_4, leading to the pollutant-plume undulation as a whole with respect to the source location. By contrast, eddies of size comparable to, but smaller than, the plume coverage result in relative dispersion, giving rise to the plume spread with respect to the instantaneous center of mass (Richardson 1926, Batchelor 1952, Monin et al. 1975, Sawford 2001, Franzese et al. 2007). Eddies, whose size is far smaller than the plume coverage, barely affect relative dispersion (Mikkelsen et al. 1987).

In the near field, the pollutant is rather horizontally homogenous in the near-ground regions (at high concentrations). As such, the small-scale eddies (IMF_1 and IMF_2) only spread the plume with respect to the instantaneous center of mass, which, however, contributes limitedly to fluctuating pollutant concentration. In the streamwise direction, three-dimensional

(3D) obstacles exist that significantly disturb the flows, enhancing plume dispersion (Li et al. 2019). Therefore, in the downstream, the large-scale pollutant plume segments into smaller, puffy air masses whose distribution is more inhomogeneous. These dynamics further facilitate small-scale eddies to pollutant mixing, augmenting fluctuating pollutant concentrations.

Figure 8 contrasts the premultiplied pollutant flux cospectrum $k_x \times \phi_{wc}$ (Nordbo et al. 2012, Vincent et al. 2013, Cheng et al. 2020) as a function of streamwise wavelength λ_x and elevation z that exhibits the streamwise scale of pollutant plume transport resulted from the turbulent transport (O'Gorman et al. 2005).

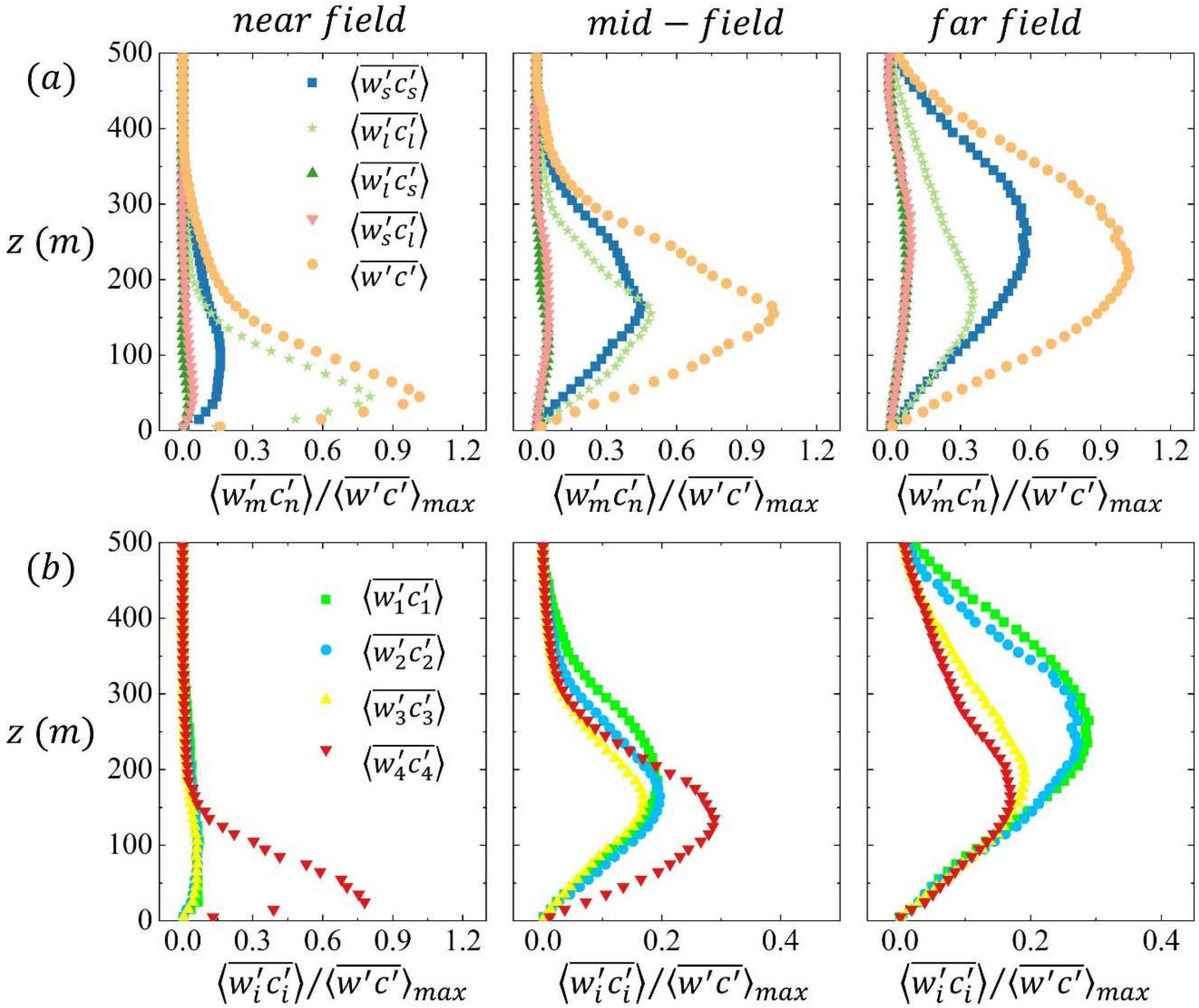

Figure 7. Contribution from (a) small or large scales and (b) different IMFs to pollutant flux $\langle\overline{w'c'}\rangle$ in the near field, mid field, and far field.

400

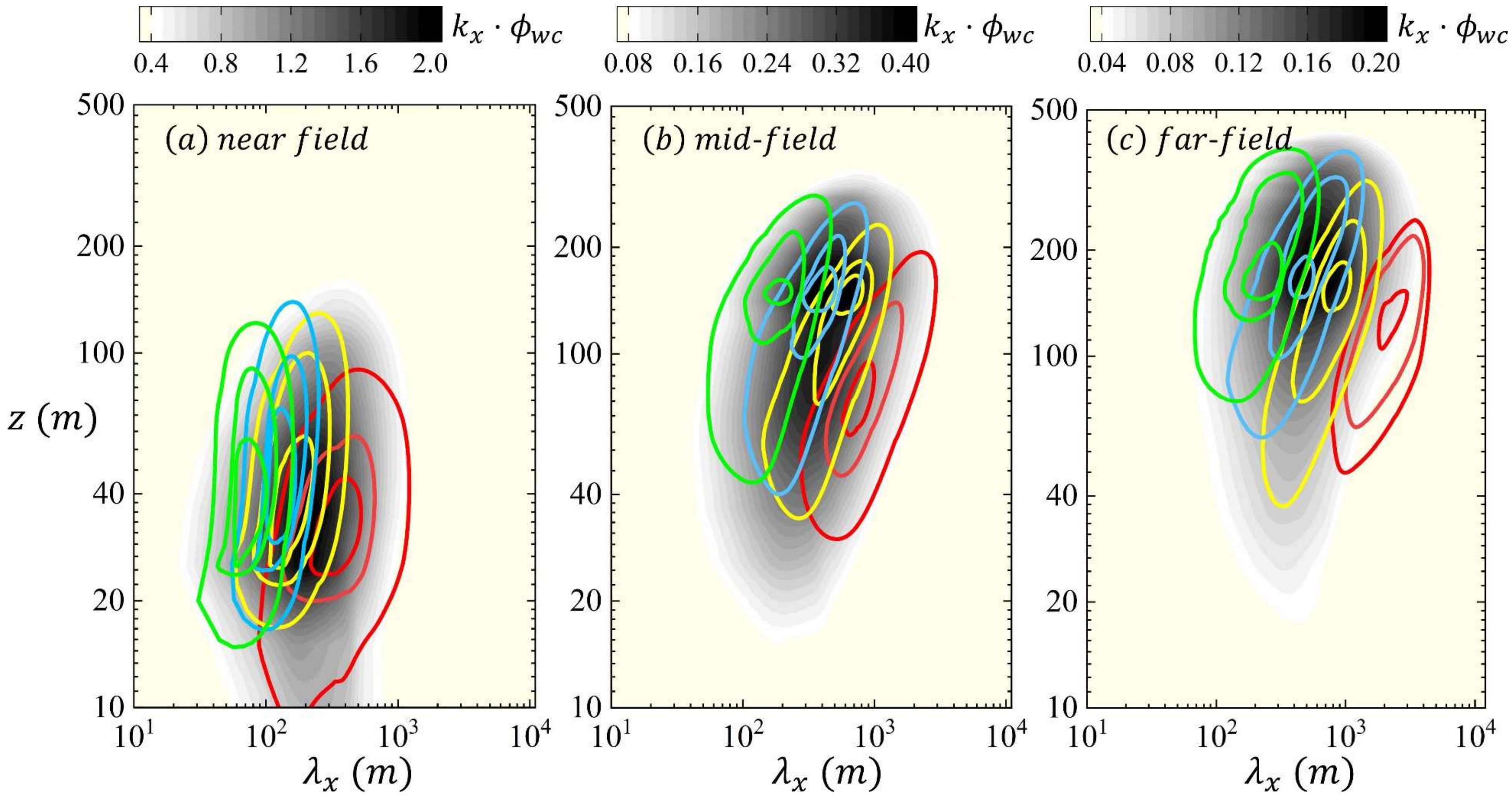

Figure 8. Premultiplied cospectrum of pollutant flux $k_x \times \phi_{wc}$ as functions of streamwise extents λ_x and elevation z in the (a) near, (b) mid, and (c) far fields. The solid lines represent levels 0.3:0.3:0.9 of different IMF cospectra, and the underlaying shaded contours (white to black) represent the cospectrum of the original signal.

401

The dispersion scale ranges from around 100 m to 1,000 m that echoes the cospectrum scale in the field measurements (Sørensen et al. 2010, Held 2014, Oliveira et al. 2018), in which the frequency is peaked in the range of 10^{-1} Hz $\leq f \leq 10^{-3}$ Hz, depending on the elevation and weather conditions. In addition, the multiscale feature of scalar transport is reported (Ramamurthy et al. 2015, Oliveira et al. 2018), where disparate dominant scales can be observed in the scalar flux cospectra. Through the EMD method, this work provides insight into different kinds of eddies to further address the multiscale features of scale transport. As shown in Figure 8, the streamwise extent of vertical pollutant flux increases with enlarging eddy size (from IMF_1 to IMF_4) and elevated location z. In the near field, most pollutants reside in the near-ground regions ($z < 60$ m; RSL), where the turbulence is mostly initiated and limited by the building blocks. The pollutant transport is determined by the near-canopy turbulence structures. Therefore, the transport scale ranges from 60 m (IMF_1) to 300 m (IMF_4) that is comparable to the separation between two high-rise buildings in the streamwise direction.

In the mid- and far-field, the pollutant concentrations fluctuate more vigorously around $z = 150$ m and 200 m, respectively. Far above the street canopy, the transport scale increases significantly that ranges from 200 m (IMF_1) to 1,500 m (IMF_4). It is noteworthy that the pollutants are transported by a wide spectrum of eddies (IMFs for flows), whose size does not change much in the streamwise (x) direction. In this connection, given the same elevation (z), the dominant motion scales of pollutant dispersion are consistent in the near, mid and far fields, though the locations of the spectral peaks are elevated downstream.

Compared with the turbulence motion scales (Figure 2), the dispersion scales are smaller or at most comparable at the same elevation z. This once again echoes that the eddies, whose size is far smaller than the plume coverage, barely affect pollutant dispersion (Mikkelsen et al. 1987). Simultaneously, the large eddies drive the plume meandering, leading to pollutant concentration fluctuations (Ardeshiri et al. 2020).

Figure 9 illustrates the horizontal view of the contribution to the vertical pollutant flux from the small (IMF_1 and IMF_2) and large (IMF_3 and IMF_4) scales at z = 50 m. The absolute value of total vertical pollutant flux $\left|\overline{w'c'}\right|$ is used to normalize the contribution that helps differentiate the positive (pollutant removal) and negative (pollutant re-entrainment or counter-gradient transport) contributions. In the upstream region, the large-scale pollutant flux $\overline{w_l'c_l'}$, which is dominated by IMF_4, plays an important role in pollutant removal, though the re-entrainment is found occasionally in some areas. This finding concurs the near-field pollutant dispersion within building clusters, where counter-gradient transport would be observed occasionally (Gousseau et al. 2015). The small-scale pollutant flux $\overline{w_s'c_s'}$ exhibits mildly in the pollutant removal and re-entrainment. However, the areas with negative $\overline{w_l'c_l'}$ expand in the downstream region, implying more frequent pollutant re-entrainment. The LSMs are larger than 100 m in the vertical that could reside/cover in the street canyons and the outer layer simultaneously. Such large eddies could help pollutant dilution (effectively) given heavy pedestrian-level pollution (Figure 9b, upstream). Whereas, there would be a drawback. They could drive the pollutants from the roof-level re-entraining down to the street canyons in case aged air accumulates in the far-field, outer layer, which trims down the roles of LSMs (Liu et al. 2005).

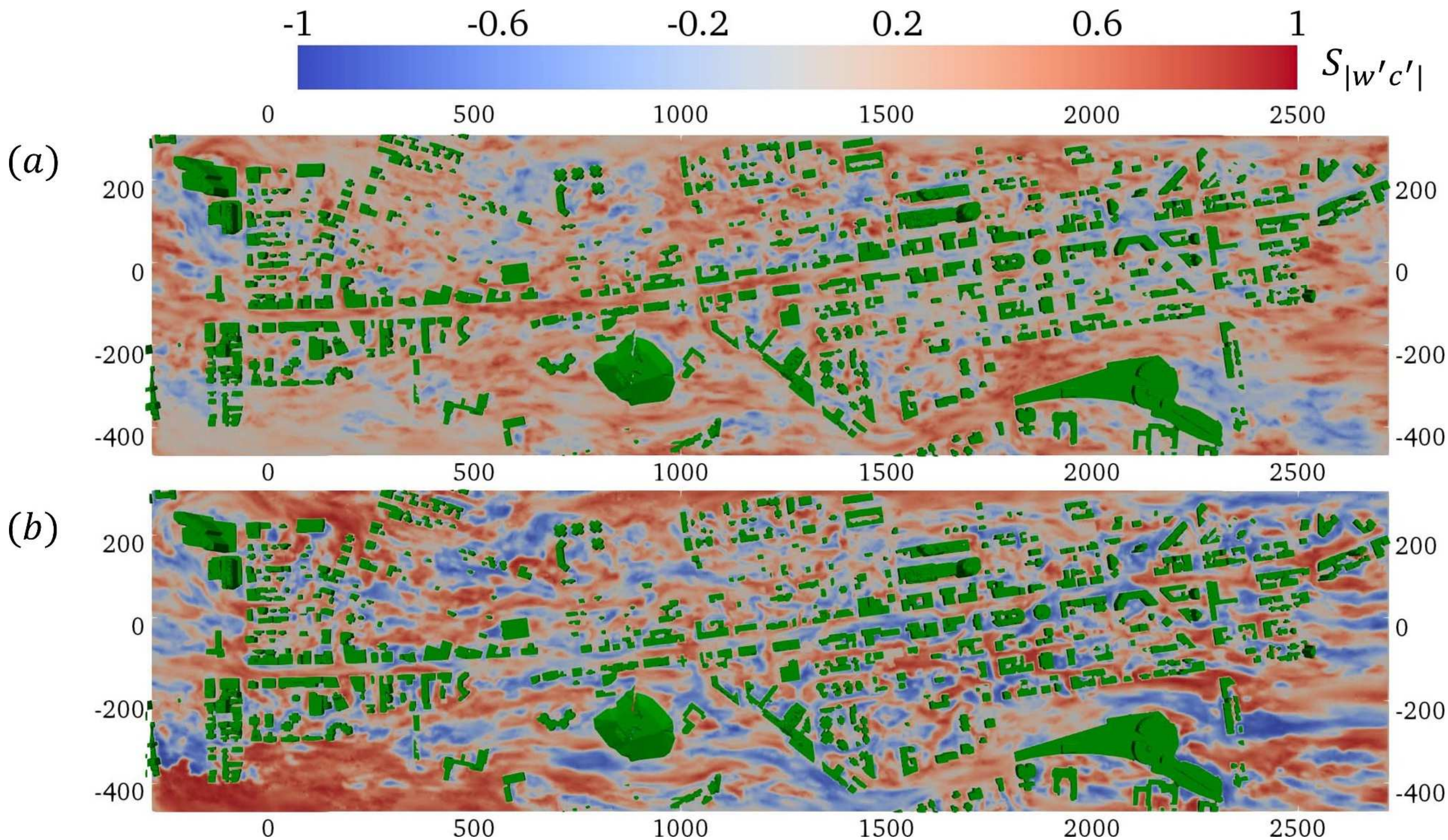

Figure 9. Horizontal view of the contribution $S_{|w'c'|}$ from (a) small scale $\overline{w_s'c_s'}/\left|\overline{w'c'}\right|$ and (b) large scale $\overline{w_l'c_l'}/\left|\overline{w'c'}\right|$ of pollutant flux at z = 50 m.

In the downstream region, the negative contribution from small-scale pollutant flux $\overline{w_s'c_s'}$ remains almost unchanged. It is mainly initiated by the buildings and the terrain (explicitly resolved roughness elements) that barely interacts with the high-concentration pollutant plume in the outer layer. However, the positive contribution from $\overline{w_s'c_s'}$ increases (Figure 9a, red color darkens). The pollutants are thus continuously disturbed by the buildings in the streamwise direction that subsequently split into small puffs. In this connection, even small-scale eddies could contribute more by carrying the inhomogeneous pollutants away from their plume centerline.

5. Practical implication

The need for effectuating pollutant-control strategy in ASLs, especially in UCLs and RSLs, arouses the concern of how to distinguish the contributions to momentum transport and pollutant dispersion from the full spectrum of turbulent motion scales. More specifically, along with the attached, small-scale eddies initiated by individual buildings and terrain, large-scale, detached motions exist that are mainly modulated by the aerodynamic resistance of the entire urban surface. Based on a building-resolved LES dataset, EMD is utilized to examine the multiscale nature of ASL turbulence over real urban morphology. The first (IMF_1) and second (IMF_2) EMD modes are able to capture the detached, small-scale eddies ($\lambda_x < \delta$) that carry the TKE components in all three directions simultaneously. Meanwhile, the third (IMF_3) and fourth (IMF_4) EMD modes collectively capture the long-streaky, detached, large-scale eddies (λ_x up to 5δ) that mainly carry the streamwise TKE.

Separating the attached and detached eddies could help evaluate their (dissimilar) roles in momentum transfer and pollutant dispersion. Compared with the small-scale ones, the large-scale eddies are found to be more efficient in transport processes especially in the settings of aligned street canyons. By contrast, the small-scale eddies show more contributions in staggered-building layout but less efficient. This finding suggests the (importance) potential of aligned-building layout to improve street-canyon wind speeds and pollutant removal. It is noteworthy that, the increased ventilation speed in the aligned street does not necessarily improve the momentum transport and pollutant removal in the vertical direction because the inflow air upstream might be polluted already, especially in large urban areas. Therefore, a compromise could be achieved between enhanced (vertical) transport and favorable pedestrian comfort. For example, the streets could be widened to avoid channeling (extremely high wind speed that degrades the wind comfort and safety) as well as promote large-scale, energetic entrainment simultaneously.

The LSMs also dominate the near-field pollutant dispersion, while other small-scale eddies have rather limited contributions. This finding could be implemented in hazard assessment of the danger in those areas being affected by accidental poison gas leakage based on different building layouts and terrain configurations, as well as the evaluation of vehicular pollutant dispersion in dense cities. In addition, in a district with aligned streets, there will usually be bystreets crossing the aligned streets at about 90° angle. This configuration often degrades the vertical transport. To avoid such unfavorable wind direction, urban planners could align streets (avenue) along the prevailing winds. Therefore, in the perspective of long-term pollutant removal performance, it is always useful to enhance the vertical transport even along aligned streets, especially when they are in the direction of the yearly prevailing wind.

6. Conclusion

With a building-resolved LES dataset over real urban morphology, we critically examine the ASL turbulence structures and their contribution to momentum transport and pollutant dispersion especially in the RSLs. The flows and pollutant concentrations are decomposed into a range of turbulence structures according to their motion scales by EMD. The small-scale eddies ($\lambda_x \leq \delta$) follow $2\lambda_y \leq \lambda_x \leq 5\lambda_y$ that could be classified as attached eddies initiated by individual buildings and terrains. These eddies carry the TKE components of all three directions that are captured by the first two EMD modes (IMF_1 and IMF_2). In contrast, the third (IMF_3) and fourth (IMF_4) EMD modes extract the large-scale eddies ($\lambda_x > \delta$) that could be classified by the detached eddies ($\lambda_x \approx 10\lambda_y$). These eddies are long, streaky structures that carry the majority streamwise TKE components $u'u'$ (up to 40%). In addition, these LSMs transport around 40% momentum flux mainly due to the rather high transport efficiency compared with the small-scale eddies.

Building configurations are found to influence the turbulence structure significantly. The aligned building configuration could promote the LSMs because the long street canyons provide the room for eddy development. Moreover, the abrupt velocity gradient resulting from the mechanical shear between buildings and mean flows produces sufficient TKE for those turbulence structures. Small-scale eddies, on the contrary, are mainly initiated by the staggering building clusters.

Finally, the large-scale structures dominate the pollutant dispersion in the near-field region, where the small-scale eddies help merely the pollutant dispersion. Because the pollutants are transported downstream, the small-scale eddies subsequently play more important roles in the pollutant dispersion. Nonetheless, the large-scale structures are responsible for nearly 40% of pollutant transport. The separation of different eddies initiated by individual buildings or city-scale street network helps improving our understanding and management of the air quality in urban areas, contributing to sustainable cities.

Acknowledgement

This research is conducted in part using the research computing facilities and/or advisory services offered by Information Technology Services (ITS), The University of Hong Kong (HKU). Technical support from Ms. Lilian Y.L. Chan, Mr. W.K. Kwan, Mr. Bill H.T. Yau and Mr. Juilian Yeung is appreciated. This study is partly supported by the Hong Kong (HK) Research Grants Council (RGC) Theme-based Research Scheme (TRS) T24-504/17-N, the HK RGC Collaborative Research Fund (CRF) C7064 18G and C5108 20G, as well as the HK RGC General Research Fund (GRF) 17209819 and 17211322.

Appendix A. Supplementary data

Figure A1 illustrates a pointwise example of the IMFs of input signal of streamwise fluctuating velocity $u'(t)$. The first IMF IMF_1 contains the minimum (local) scale properties of the original signal. As the IMF (mode) number increases, the IMFs gradually shift from the local-scale information to the global one.

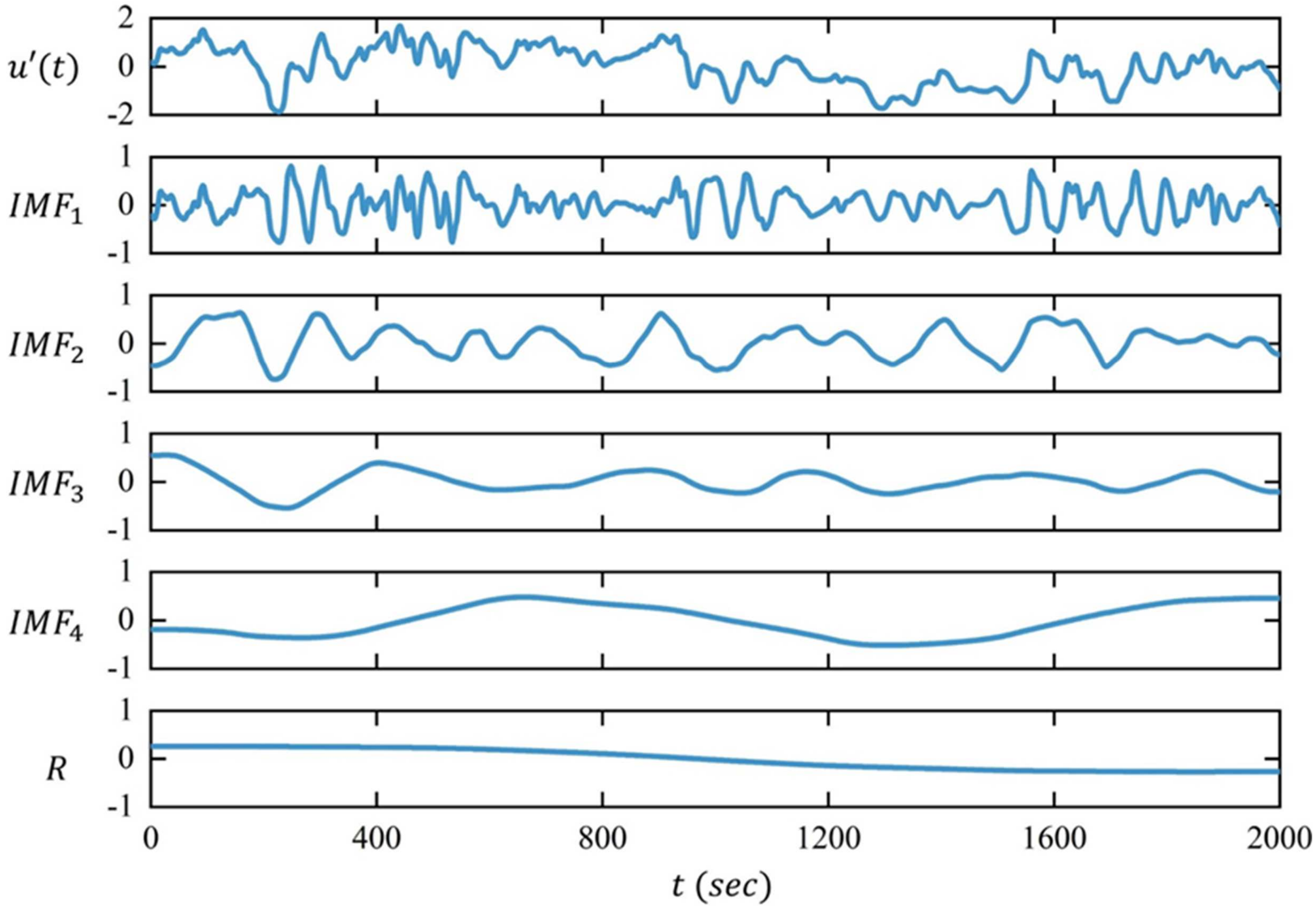

Figure A1. Pointwise example of EMD: the original signal $u'(t)$, IMF_i components, and residual R.

538

References

Agostini, L., et al. (2018). "The Impact of Footprints of Large-Scale Outer Structures on the Near-Wall Layer in the Presence of Drag-Reducing Spanwise Wall Motion." Flow, Turbulence and Combustion 100(4): 1037-1061.

Anderson, W. (2016). "Amplitude modulation of streamwise velocity fluctuations in the roughness sublayer: evidence from large-eddy simulations." Journal of Fluid Mechanics 789: 567-588.

Antoniou, N., et al. (2017). "CFD and wind-tunnel analysis of outdoor ventilation in a real compact heterogeneous urban area: Evaluation using “air delay”." Building and Environment 126: 355-372.

Ardeshiri, H., et al. (2020). "On the Convergence and Capability of the Large-Eddy Simulation of Concentration Fluctuations in Passive Plumes for a Neutral Boundary Layer at Infinite Reynolds Number." Boundary-Layer Meteorology 176(3): 291-327.

Aristodemou, E., et al. (2018). "How tall buildings affect turbulent air flows and dispersion of pollution within a neighbourhood." Environmental Pollution 233: 782-796.

Auvinen, M., et al. (2020). "Study of Realistic Urban Boundary Layer Turbulence with High-Resolution Large-Eddy Simulation." Atmosphere 11(2).

Batchelor, G. K. (1952). "Diffusion in a field of homogeneous turbulence: II. The relative motion of particles." Mathematical Proceedings of the Cambridge Philosophical Society 48(2): 345-362.

Bernardini, M., et al. (2014). "Velocity statistics in turbulent channel flow up to Re-tau=4000." Journal of Fluid Mechanics 742: 171-191.

Cassiani, M., et al. (2009). "A coupled Eulerian and Lagrangian mixing model for intermittent concentration time series." Physics of fluids (1994) 21(8): 85105.

Cheng, C., et al. (2019). "Identity of attached eddies in turbulent channel flows with bidimensional empirical mode decomposition." Journal of Fluid Mechanics 870: 1037-1071.

Cheng, W.-C., et al. (2021). Turbulent flows over real heterogeneous urban surfaces: Wind tunnel experiments and Reynolds-averaged Navier-Stokes simulations. Building simulation, Springer.

Cheng, X. X., et al. (2017). "A Study of Nonstationary Wind Effects on a Full-Scale Large Cooling Tower Using Empirical Mode Decomposition." Mathematical problems in engineering 2017: 1-15.

Cheng, Y., et al. (2020). "Power-Law Scaling of Turbulence Cospectra for the Stably Stratified Atmospheric Boundary Layer." Boundary-Layer Meteorology 177(1): 1-18.

Csanady, G. T. (1973). Turbulent diffusion in the environment. Dordrecht, Reidel.

Debert, S., et al. (2010). "Ensemble-Empirical-Mode-Decomposition method for instantaneous spatial-multi-scale decomposition of wall-pressure fluctuations under a turbulent flow." Experiments in Fluids 50(2): 339-350.

del ÁLamo, J. C., et al. (2006). "Self-similar vortex clusters in the turbulent logarithmic region." Journal of Fluid Mechanics 561: 329-358.

Deshpande, R., et al. (2019). "Streamwise inclination angle of large wall-attached structures in turbulent boundary layers." Journal of Fluid Mechanics 877.

Duan, G., et al. (2021). "Predicting Urban Surface Roughness Aerodynamic Parameters Using Random Forest." Journal of Applied Meteorology and Climatology 60(7): 999-1018.

Duan, Y., et al. (2020). "Contributions of very large-scale motions to turbulence statistics in open channel flows." Journal of Fluid Mechanics 892.

Duan, Y., et al. (2021). "Contributions of different scales of turbulent motions to the mean wall-shear stress in open channel flows at low-to-moderate Reynolds numbers." Journal of Fluid Mechanics 918.

Encinar, M. P., et al. (2020). "Momentum transfer by linearised eddies in turbulent channel flows." Journal of Fluid Mechanics 895.

Fan, Y., et al. (2022). "Decomposition of the mean friction drag on an NACA4412 airfoil under uniform blowing/suction." Journal of Fluid Mechanics 932.

Fang, J., et al. (2015). "Large-Eddy Simulation of Very-Large-Scale Motions in the Neutrally Stratified Atmospheric Boundary Layer." Boundary-Layer Meteorology 155(3): 397-416.

Fesquet, C., et al. (2009). "Impact of terrain heterogeneity on near-surface turbulence structure." Atmospheric Research 94(2): 254-269.

Franzese, P., et al. (2007). "A statistical theory of turbulent relative dispersion." Journal of Fluid Mechanics 571: 391-417.

Fu, X., et al. (2020). "High-resolution simulation of local traffic-related NOx dispersion and distribution in a complex urban terrain." Environmental Pollution 263: 114390.

Gao, Z., et al. (2016). "Large eddies modulating flux convergence and divergence in a disturbed unstable atmospheric surface layer: LARGE EDDIES MODULATING FLUX." Journal of geophysical research. Atmospheres 121(4): 1475-1492.

Gifford, F. (1959). Statistical Properties of A Fluctuating Plume Dispersion Model. Advances in Geophysics. H. E. Landsberg and J. Van Mieghem, Elsevier. 6: 117-137.

Gousseau, P., et al. (2012). "Large-Eddy Simulation of pollutant dispersion around a cubical building: analysis of the turbulent mass transport mechanism by unsteady concentration and velocity statistics." Environmental Pollution 167: 47-57.

Gousseau, P., et al. (2015). "Near-field pollutant dispersion in an actual urban area: Analysis of the mass transport mechanism by high-resolution Large Eddy Simulations." Computers & Fluids 114: 151-162.

Hang, J., et al. (2017). "The influence of street layouts and viaduct settings on daily carbon monoxide exposure and intake fraction in idealized urban canyons." Environmental Pollution 220: 72-86.

Hawinkel, P., et al. (2015). "A time series processing tool to extract climate-driven interannual vegetation dynamics using Ensemble Empirical Mode Decomposition (EEMD)." Remote Sensing of Environment 169: 375-389.

Held, A. (2013). "Spectral Analysis of Turbulent Aerosol Fluxes by Fourier Transform, Wavelet Analysis, and Multiresolution Decomposition." Boundary-Layer Meteorology 151(1): 79-94.

Held, A. (2014). "Spectral Analysis of Turbulent Aerosol Fluxes by Fourier Transform, Wavelet Analysis, and Multiresolution Decomposition." Boundary-Layer Meteorology 151(1): 79-94.

Hertwig, D., et al. (2019). "Wake Characteristics of Tall Buildings in a Realistic Urban Canopy." Boundary-Layer Meteorology 172(2): 239-270.

Horiguchi, M., et al. (2012). "Large-Scale Turbulence Structures and Their Contributions to the Momentum Flux and Turbulence in the Near-Neutral Atmospheric Boundary Layer Observed from a 213-m Tall Meteorological Tower." Boundary-Layer Meteorology 144(2): 179-198.

Horiguchi, M., et al. (2022). "Large-Scale Turbulence Structures in the Atmospheric Boundary Layer Observed above the Suburbs of Kyoto City, Japan." Boundary-Layer Meteorology 184(2): 333-354.

Hu, R., et al. (2020). "Wall-attached and wall-detached eddies in wall-bounded turbulent flows." Journal of Fluid Mechanics 885.

Huang, N. E., et al. (1998). "The empirical mode decomposition and the Hilbert spectrum for nonlinear and non-stationary time series analysis." Proceedings of the Royal Society.

A, Mathematical, physical, and engineering sciences 454(1971): 903-995.

Hwang, Y. (2015). "Statistical structure of self-sustaining attached eddies in turbulent channel flow." Journal of Fluid Mechanics 767: 254-289.

Inagaki, A., et al. (2017). "A Numerical Study of Turbulence Statistics and the Structure of a Spatially-Developing Boundary Layer Over a Realistic Urban Geometry." Boundary-Layer Meteorology 164(2): 161-181.

Jacobi, I., et al. (2021). "Interactions between scales in wall turbulence: phase relationships, amplitude modulation and the importance of critical layers." Journal of Fluid Mechanics 914.

Jadidi, M., et al. (2017). "Scale-adaptive simulation of unsteady flow and dispersion around a model building: spectral and POD analyses." Journal of Building Performance Simulation 11(2): 241-260.

Jiang, G., et al. (2018). "Large-eddy simulation of flow and pollutant dispersion in a 3D urban street model located in an unstable boundary layer." Building and Environment 142: 47-57.

Jiménez, J. (2018). "Coherent structures in wall-bounded turbulence." Journal of Fluid Mechanics 842.

Kim, T., et al. (2020). "Experimental evidence of amplitude modulation in permeable-wall turbulence." Journal of Fluid Mechanics 887.

Lateb, M., et al. (2016). "On the use of numerical modelling for near-field pollutant dispersion in urban environments − A review." Environmental Pollution 208: 271-283.

Lee, J., et al. (2014). "Spatial organization of large- and very-large-scale motions in a turbulent channel flow." Journal of Fluid Mechanics 749: 818-840.

Li, Q., et al. (2019). "Contrasts between momentum and scalar transport over very rough surfaces." Journal of Fluid Mechanics 880: 32-58.

Li, X.-X., et al. (2006). "Recent progress in CFD modelling of wind field and pollutant transport in street canyons." Atmospheric Environment 40(29): 5640-5658.

Li, X., et al. (2021). "Turbulent/Synoptic Separation and Coherent Structures in the Atmospheric Surface Layer for a Range of Surface Roughness." Boundary-Layer Meteorology 182(1): 75-93.

Liu, C.-H., Leung, D.Y.C. and Barth, M.C. (2005). “On the prediction of air and pollutant exchange rates in street canyons of different aspect ratios using large-eddy simulation.” Atmospheric Environment 39: 1567-1574.

Liu, H., et al. (2019). "Amplitude modulation between multi-scale turbulent motions in high-Reynolds-number atmospheric surface layers." Journal of Fluid Mechanics 861: 585-607.

Liu, Y., et al. (2023a). "Wavelet analysis of the atmospheric flows over real urban morphology." Science of the Total Environment 859: 160209.

Liu, Y., et al. (2023b). "Proper orthogonal decomposition of large-eddy simulation data over real urban morphology." Sustainable Cities and Society 89: 104324.

Liu, Y., et al. (2023c). “Amplitude modulation of velocity fluctuations in the atmospheric flows over real urban morphology.”, Physics of Fluids 35: 025116.

Lotfy, E. R., et al. (2019). "Characteristics of Turbulent Coherent Structures in Atmospheric Flow Under Different Shear–Buoyancy Conditions." Boundary-Layer Meteorology 173(1): 115-141.

Lv, Y., et al. (2016). "Multivariate empirical mode decomposition and its application to fault diagnosis of rolling bearing." Mechanical systems and signal processing 81: 219-234.

Martins, L. G. N., et al. (2016). "Using Empirical Mode Decomposition to Filter Out Non-turbulent Contributions to Air–Sea Fluxes." Boundary-Layer Meteorology 163(1): 123-141.

Masoumi-Verki, S., et al. (2021). "Embedded LES of thermal stratification effects on the airflow and concentration fields around an isolated high-rise building: Spectral and POD analyses." Building and Environment 206.

Mäteling, E., et al. (2020). "Detection of small-scale/large-scale interactions in turbulent wall-bounded flows." Physical Review Fluids 5(11).

Mathis, R., et al. (2009). "Large-scale amplitude modulation of the small-scale structures in turbulent boundary layers." Journal of Fluid Mechanics 628: 311-337.

Meng, L., et al. (2015). "A hybrid fault diagnosis method using morphological filter–translation invariant wavelet and improved ensemble empirical mode decomposition." Mechanical systems and signal processing 50-51: 101-115.

Michioka, T., et al. (2011). "Wind-Tunnel Experiments for Gas Dispersion in an Atmospheric Boundary Layer with Large-Scale Turbulent Motion." Boundary-Layer Meteorology 141(1): 35-51.

Mikkelsen, T., et al. (1987). "Diffusion of Gaussian Puffs." Quarterly Journal of the Royal Meteorological Society 113: 81-105.

Mo, Z., et al. (2021). “Roughness sublayer flows over real urban morphology: A wind tunnel study”. Building and Environment, 188: 107463,

Monin, A. S., et al. (1975). Statistical Fluid Mechanics: Mechanics of Turbulence, MIT Press.

Nordbo, A., et al. (2012). "A Wavelet-Based Correction Method for Eddy-Covariance High-Frequency Losses in Scalar Concentration Measurements." Boundary-Layer Meteorology 146(1): 81-102.

O'Gorman, P. A., et al. (2005). "Effect of Schmidt number on the velocity–scalar cospectrum in isotropic turbulence with a mean scalar gradient." Journal of Fluid Mechanics 532: 111-140.

Oladosu, G. (2009). "Identifying the oil price–macroeconomy relationship: An empirical mode decomposition analysis of US data." Energy Policy 37(12): 5417-5426.

Oliveira, P. E. S., et al. (2018). "Nighttime wind and scalar variability within and above an Amazonian canopy." Atmos. Chem. Phys. 18(5): 3083-3099.

Perret, L., et al. (2013). "Large-Scale Structures over a Single Street Canyon Immersed in an Urban-Type Boundary Layer." Boundary-Layer Meteorology 148(1): 111-131.

Ramamurthy, P., et al. (2015). "Turbulent Transport of Carbon Dioxide over a Highly Vegetated Suburban Neighbourhood." Boundary-Layer Meteorology 157(3): 461-479.

Rehman, N., et al. (2010). "Multivariate empirical mode decomposition." 466(2117): 1291-1302.

Richardson, L. F. (1926). "Atmospheric diffusion shown on a distance-neighbour graph." Proceedings of the Royal Society of London. Series A, Containing papers of a mathematical and physical character 110(756): 709-737.

Rilling, G., et al. (2007). "Bivariate Empirical Mode Decomposition." IEEE signal processing letters 14(12): 936-939.

Salesky, S. T., et al. (2018). "Buoyancy effects on large-scale motions in convective atmospheric boundary layers: implications for modulation of near-wall processes." Journal of Fluid Mechanics 856: 135-168.

Sawford, B. (2001). "TURBULENT RELATIVE DISPERSION." Annual Review of Fluid Mechanics 33(1): 289-317.

Sørensen, L. L., et al. (2010). "Atmosphere–Surface Fluxes of CO2 using Spectral Techniques." Boundary-Layer Meteorology 136(1): 59-81.

Talluru, K. M., et al. (2014). "Amplitude modulation of all three velocity components in turbulent boundary layers." Journal of Fluid Mechanics 746.

Tang, Z., et al. (2020). "Tomographic particle image velocimetry flow structures downstream of a dynamic cylindrical element in a turbulent boundary layer by multi-scale proper orthogonal decomposition." Physics of Fluids 32(12).

Tang, Z., et al. (2019). "Local dynamic perturbation effects on amplitude modulation in turbulent boundary layer flow based on triple decomposition." Physics of Fluids 31(2).

Thirumalaisamy, M. R., et al. (2018). "Fast and Adaptive Empirical Mode Decomposition for Multidimensional, Multivariate Signals." IEEE signal processing letters 25(10): 1550-1554.

Tominaga, Y., et al. (2008). "AIJ guidelines for practical applications of CFD to pedestrian wind environment around buildings." Journal of Wind Engineering and Industrial Aerodynamics 96(10): 1749-1761.

Tominaga, Y., et al. (2013). "CFD simulation of near-field pollutant dispersion in the urban environment: A review of current modeling techniques." Atmospheric environment (1994) 79: 716-730.

Townsend, A. A. (1976). The structure of turbulent shear flow. Cambridge, Cambridge University Press.

Vincent, C. L., et al. (2013). "Cross-Spectra Over the Sea from Observations and Mesoscale Modelling." Boundary-Layer Meteorology 146(2): 297-318.

Vinuesa, J.-F., et al. (2009). "Turbulent Dispersion of Non-uniformly Emitted Passive Tracers in the Convective Boundary Layer." Boundary-Layer Meteorology 133(1): 1-16.

Vinuesa, R., et al. (2016). "Convergence of numerical simulations of turbulent wall-bounded flows and mean cross-flow structure of rectangular ducts." Meccanica (Milan) 51(12): 3025-3042.

Wang, G., et al. (2014). "Transition region where the large-scale and very large scale motions coexist in atmospheric surface layer: wind tunnel investigation." Journal of Turbulence 15(3): 172-185.

Wang, G., et al. (2016). "Very large scale motions in the atmospheric surface layer: a field investigation." Journal of Fluid Mechanics 802: 464-489.

Wang, W., et al. (2017). "Quasi-bivariate variational mode decomposition as a tool of scale analysis in wall-bounded turbulence." Experiments in Fluids 59(1): 1-18.

Wang, W., et al. (2019). "Multi-component variational mode decomposition and its application on wall-bounded turbulence." Experiments in Fluids 60(6): 1-16.

Wu, Z., et al. (2018). "Budget analysis for reactive plume transport over idealised urban areas." Geoscience Letters 5(1): 19.

Yao, L., et al. (2022). "Statistical analysis of the organized turbulence structure in the inertial and roughness sublayers over real urban area by building-resolved large-eddy simulation." Building and Environment 207: 108464.

Zhang, Z.-L., et al. (2019). "Characteristics of large- and small-scale structures in the turbulent boundary layer over a drag-reducing riblet surface." Proceedings of the Institution of Mechanical Engineers, Part C: Journal of Mechanical Engineering Science 234(3): 796-807.

Zheng, X., et al. (2021). "CFD simulations of wind flow and pollutant dispersion in a street canyon with traffic flow: Comparison between RANS and LES." Sustainable cities and society 75: 103307.

Zhong, J., et al. (2015). "Modelling the dispersion and transport of reactive pollutants in a deep urban street canyon: Using large-eddy simulation." Environmental Pollution 200: 42-52.